On the need of a scale-dependent material characterization to describe the mechanical behavior of 3D printed Ti6Al4V custom prostheses using finite element models

Francesca Danielli [a,1], Luca Ciriello [a,1], Luigi La Barbera [a,b,*], Jose Felix Rodriguez Matas [a], Giancarlo Pennati [a]

[a] LaBS – Laboratory of Biological Structure Mechanics, Department of Chemistry, Materials and Chemical Engineering "Giulio Natta", Politecnico di Milano, Italy
[b] IRCCS Istituto Ortopedico Galeazzi, Italy

ARTICLE INFO

ABSTRACT

Additive manufacturing is widely used in the orthopaedic industry for the high freedom and flexibility in the design and production of personalized custom implants made of Ti6Al4V. Within this context, finite element modeling of 3D printed prostheses is a robust tool both to guide the design phase and to support clinical evaluations, possibly virtually describing the in-vivo behavior of the implant. Given realistic scenarios, a suitable description of the overall implant's mechanical behavior is unavoidable. Considering typical custom prostheses' designs (i.e. acetabular and hemipelvis implants), complex designs involving solid and/or trabeculated parts, and material distribution at different scales hinder a high-fidelity modeling of the prostheses.

Moreover, uncertainties in the production and in the material characterization of small parts approaching the accuracy limit of the additive manufacturing technology still exist.

While recent works suggest that the mechanical properties of thin 3D-printed parts may be peculiarly affected by specific processing parameters (i.e. powder grain size, printing orientation, samples' thickness) as compared to conventional Ti6Al4V alloy, the current numerical models make gross simplifications in describing the complex material behavior of each part at different scales.

The present study focuses on two patient-specific acetabular and hemipelvis prostheses, with the aim of experimentally characterizing and numerically describing the dependency of the mechanical behavior of 3D printed parts on their peculiar scale, therefore, overcoming one major limitation of current numerical models. Coupling experimental activities with finite element analyses, the authors initially characterized 3D printed Ti6Al4V dog-bone samples at different scales, representative of the main material components of the investigated prostheses. Afterwards, the authors implemented the characterized material behaviors into finite element models to compare the implications of adopting scale-dependent vs. conventional scaleindependent approaches in predicting the experimental mechanical behavior of the prostheses in terms of their overall stiffness and the local strain distribution. The material characterization results highlighted the need for a scale-dependent reduction of the elastic modulus for thin samples compared to the conventional Ti6Al4V, which is fundamental to properly describe the overall stiffness and local strain distribution on the prostheses.

The presented works demonstrate how an appropriate material characterization and a scale-dependent material description is needed to develop reliable FE models of 3D printed implants characterized by a complex material distribution at different scales.

1. Introduction

Additive Manufacturing is a 3D printing technology in which a

material powder (metal or plastic) is deposited layer by layer to manufacture 3D physical objects starting from Computer-Aided Design (CAD) models. Since its appearance in the 1980s, it has become a well-stated manufacturing process today, gaining importance in the personalized medicine industry during the last decade (Li et al., 2020; Kumar et al., 2021). Within this scenario, metal orthopedic prostheses represent a clear example of 3D-printed applications. As compared to conventional manufacturing technologies (i.e. forging), high freedom is allowed in the design and production of custom devices that properly fit anatomical sites characterized by complex morphologies, such as the human pelvis (Javaid and Haleem, 2018; Hilton et al., 2017; Wong et al., 2015).

Fig. 1a shows two examples of custom orthopedic 3D-printed implants: an acetabular (Fig. 1a, left) and a hemipelvis prosthesis (Fig. 1a, right). As for traditionally manufactured prostheses, a suitable fixture is present to allow anchoring the implant to the surrounding healthy bone. Screws are used to fix the protheses to the bone, providing the primary stability of the implant. In addition, solid parts are present as an external shell (*Shell Structure*), which has different functionalities according to the anatomical site of interest. For instance, it may act as an articular surface with respect to the surrounding bone tissues, as for a knee prosthesis, or they may interface with the viscera of the abdominal cavity, as for a hemipelvis prosthesis (Fig. 1a, right). Lattice structures

are introduced in the design with two objectives: i) to be used as trabecular fillers (*Trabecular Filler*) to reduce the implant's weight while providing the implant with a stiffness that approaches the stiffness of native bone structures, thus avoiding the stress-shielding phenomenon; ii) to provide superior osteoconductive properties at the bone-implant interface (*Trabecular Interface*), promoting bone ingrowth, thus providing secondary stability (Iqbal et al., 2017).

Within this context, Finite Element (FE) analysis may be a reliable tool in guiding the design of a 3D-printed custom prosthesis, functionally evaluating the biomechanics of bone-prosthesis coupling, and supporting preclinical evaluations (Iqbal et al., 2017; Yan et al., 2020; Pianigiani and Verga, 2021). In this regard, a suitable description of the overall implant's stiffness, thus a correct load transmission to the surrounding bone, is fundamental. Looking at a prosthesis design described above, several details need to be encompassed, such as the distribution of the trabecular filler, the optimal positioning of the fixation points, or the right dimensioning of the shell structure, among others. The presence of trabeculated parts hinders the FE modeling of the overall prosthesis, resulting in a significant computation effort if each trabecula is discretized using many 3D elements. A more convenient strategy is based on the Asymptotic Expansion Homogenization (AEH), exhaustively described in previous works (Ghosh et al., 1996), according to which the effective mechanical properties of an inhomogeneous trabecular part are related to a continuum medium through a homogenized stiffness matrix. Looking at the literature, the majority of studies that focus on FE modeling of trabecular orthopedic prostheses or simply of lattice structures do not describe the trabeculated parts in detail (Rahimizadeh et al., 2018; La Barbera et al., 2019; El Halabi et al., 2011; Arabnejad et al., 2017; Wang et al., 2018). Despite the advantage of reduced computation times, AEH assumes that the trabecular cell unit has an infinitely periodic distribution in space, a hypothesis that may be inaccurate in the presence of limited in number and incomplete cells.

Moving from purely numerical aspects to manufacturing features, issues related to particularities of 3D-printing production, such as the mechanical behavior of small volumes (i.e. lattice structures with strut thicknesses in the order of hundreds of microns), are not addressed. Nonetheless, this topic is currently an ongoing research field with still
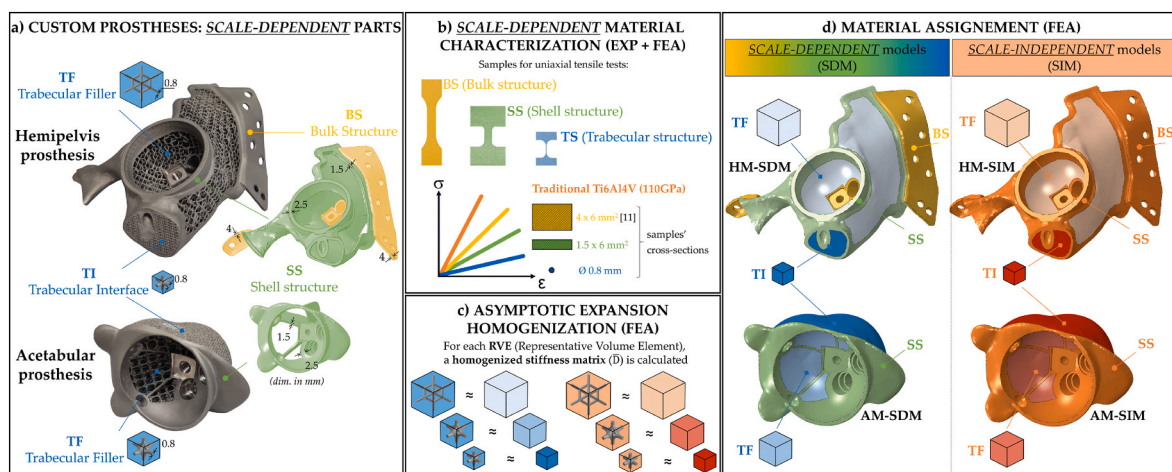

Fig. 1. Schematic representation of the proposed approach to develop FE models of custom orthopedic prostheses produced by EBM. (a) Physical samples of hemipelvis (top left) and acetabular (bottom left) prostheses, where the relevant metal structures are highlighted with their typical dimensions quoted: Trabecular Filler (TF), Interface Filler (IF), Shell Structure (SS), and solid Bulk Structures (BS). All trabecular parts (TF and TI) have a circular cross-section with a nominal diameter of 0.8 mm; SS parts have a variable cross-section (average thickness range: 1.5 ÷ 2.5 mm); BS parts have a variable cross-section (average thickness range 2.5 ÷ 4.0 mm). (b) Scale-dependent material characterization through experimental (EXP) uniaxial tensile tests coupled with Finite Element Analyses (FEA) for each sample representative of each relevant metal structures of the prostheses: the force-displacement curves were post-processed and the elastic modulus was extracted (E). (c) The trabeculated parts were modeled as continuum solids exploiting the Asymptotic Expansion Homogenization (AEH) algorithm (Ghosh et al., 1996; La Barbera et al., 2019; El Halabi et al., 2011). (d) The identified material parameters were assigned to each part of both the hemipelvis model (HM) and acetabular models (AM) comparing accurate scale-dependent models (SDM) based on a scale-dependent material characterization vs. traditional scale-independent models (SIM) based on traditional material properties without accounting for the scale-effect on E. Please, refer to the electronic on-line version of this article to appreciate the color code.

open issues on the so-called *size-effect*. Indeed, looking at the literature, recent works suggest how the mechanical properties of thin 3D-printed thin products (elastic modulus, yield strength, ultimate tensile strength, and fatigue performance) may be affected by the grain size of the powder, the thickness, and printing orientation of the samples themselves, due to a combination of microstructural changes and an increased presence of superficial and internal defects (Sergueeva et al., 2009; Dzugan et al., 2018; Murchio et al., 2021; De Luca et al., 2021; Phutela et al., 2020). For instance, Murchio et al. (2021) investigated Ti6Al4V specimens with a nominal diameter of 0.6 mm, approaching the typical thickness of bone trabeculae (range: $200 \div 1000$ µm (Ho et al., 2013; Turunen et al., 2020)), manufactured by laser powder bed fusion, and they found an elastic modulus significantly reduced by 30% compared to conventional Ti6Al4V. Similarly, Dzougan et al. (Dzugan et al., 2018) found a consistent reduction up to 40% for Ti6Al4V specimens realized via selective laser melting with a nominal diameter of 0.6 mm.

Despite this evidence, the works focusing on FE analysis of orthopedic prostheses do not consider this size-effect when modeling implants with trabecular parts. Indeed, conventional Ti6Al4V is assigned to solid parts and trabecular structures (Rahimizadeh et al., 2018; Wojnicz et al., 2021; Moussa et al., 2020; Mehboob et al., 2020). This represents an approximation that could lead to significant errors when evaluating the mechanical behavior of the prosthesis and the effects on the surrounding bone, especially at the interface with the bone, where thin trabecular structures are needed.

This study investigates the influence that the mechanical properties of different structures of the prosthesis, i.e. solid and trabecular structures, have on its overall stiffness. Two patient-specific orthopedic implants were the object of the study: namely, an acetabular and a hemipelvis prosthesis, involving complex geometries and material distribution, were investigated by comparing the proposed approach with the above-cited literature. Specific aims of this study were: i) to characterize 3D printed dog-bone samples at the same scales as the main metal components of the prosthesis, ii) to develop reliable FE models for each patient-specific prosthesis, involving a description of the material heterogeneity, and iii) to investigate the implant stiffness and load distribution among the different metal structures, by comparison between laboratory experiments and numerical simulations. The workflow of the current study is depicted in Fig. 1.

2. Materials and methods

The activities involved the manufacturing and testing of 3D printed samples: dog-bone specimens to characterize the material at different scales, and two custom implants to evaluate their stiffness. Adler Ortho SPA (Cormano, Italy) 3D-printed all the products using an Electron Beam Melting (EBM) system (Arcam, Mölndal, Sweden). Ti6Al4V ELI (grade 23) was used as a metal.

2.1. Material characterization at different scales

Given the complexity of 3D printed orthopedic devices discussed in the **Introduction**, a material characterization at different scales is needed to describe each metal structure featuring the implants correctly. For the specific applications, the main scales involved are the following. i) The *Trabecular Structures* (indicated as *TS* in the following) used as both fillers and implant-bone interfaces are cylindrical struts with a nominal diameter of 0.8 mm; ii) the *Shell-Structures* (indicated as *SS* in the following) are fully-solid shell-like parts with an average thickness in the range $0.5 \div 2.5$ mm; iii) the *Bulk Structures* (indicated as *BS* in the following), used as both fixing- and bearing-systems, are fully-solid parts with thickness larger than 2.5 mm. Based on the identified scales, dog-bone specimens with cross-section dimensions in the range of the *TS* and *SS* were manufactured to assess the size effect expected with 3D-printed materials structures having a variable size also approaching

the technical limits (i.e. layer thickness and particle size of the metal powder) of the 3D printing technique (Murchio et al., 2021). Namely, the following batches were manufactured: i) 3 specimens with a circular cross-section, a nominal diameter of 0.8 mm, and a gauge length of 8 mm (namely, *TS_1, TS_2, TS_3*) (Fig. 2a); ii) 3 specimens with a rectangular cross-section 6×1.5 mm and a gauge length of 8 mm (namely, *SS_1, SS_2, SS_3*) (Fig. 2b). It is worth mentioning that manufactured samples were printed perpendicular to the building platform of the 3D printer (Fig. 2). Regarding the specimens resembling the dimension of *BS*, 6 mm × 4 mm rectangular samples were characterized in a previous work (La Barbera et al., 2019). Following the manufacturing phase, uniaxial tests were performed and adequately post-processed.

2.1.1. Experimental tests

Uniaxial tensile tests (Fig. 2c) were performed to identify the elastic modulus for each specimen. The samples were loaded in displacement control using an *MTS 858 MiniBionix testing machine* (MTS System Inc., Minneapolis, MN), imposing a rate of 1 mm/min, and the forces were recorded. The small samples' gauge length prevented using extensometers to measure the strains. Therefore, the approach described in the following section was used to calculate the strain.

2.1.2. Post-processing of experimental data

The identification of the elastic modulus (E) must come through the calculation of the stress (σ), and the deformation (ε) experienced within the gauge length ($E = \frac{\sigma}{\varepsilon}$). σ is calculated as $\sigma = \frac{F_{EXP}}{A_{L0}}$, where F_{EXP} is the applied axial load and A_{L0} is the initial circular cross-section area of the specimen. Works available in the literature highlighted the presence of mismatches between a 3D printed product and the corresponding nominal geometry, especially with regard to thin struts, as reported in Murchio et al. (2021). To minimize the uncertainties in the calculation of A_{L0}, optical measurements were performed to evaluate the actual dimensions of the cross-sections (Fig. 2d). The diameter of *TS* samples and both the width and thickness of *SS* samples were measured using *Canon EOS 6D* digital camera (20.2 MP) with 5X magnification together with the *ImageJ* (Wayne Rasband, National Institutes of Health, USA) software. For each specimen, 20 measures at equally spaced intervals of 0.4 mm were taken over the gauge length of 8 mm, and the average and the standard deviation were calculated. Given the uncertainties in the manufacturing of thin samples, measurements were taken from four different sides of the dog-bones (rotating the samples by 45° for each set of measures). The measurements were performed on the samples before the uniaxial test.

For calculating the deformation within the gauge length (L_0), a FE Analysis (FEA) of the experimental test was performed; the actual dimension of the dog-bones and the distance between grips used on the actual test were considered in the simulations. Then, the deformation of the gauge length, ε, was computed as (1):

$$\varepsilon = \frac{u_{L0_{FEA}}}{u_{tot_{FEA}}} \frac{u_{tot_{EXP}}}{L_0}, \tag{1}$$

where $u_{L0_{FEA}}$ and $u_{tot_{FEA}}$ are the displacement of the gauge length and the displacement between grips obtained from the FEM analysis respectively, and $u_{tot_{EXP}}$ is the displacement between grips in the experimental test. The numerical quantities have been calculated extracting the nodal displacements from a node path defined along the gauge length of the samples.

Prior to the current study, the FEA approach was assessed by performing the DIC (Digital Image Correlation) analysis, given the infeasibility of using strain gauges due to the small dimensions of the tested samples. Namely, two batches of dog bone samples were produced with the same printing technology used in this study (dimension 8 mm gauge length, and both 6×1.5 mm^2 and 1.5×1.5 mm^2 cross-section) and tested as described in paragraph 2.1.1. Thanks to the natural roughness of thin 3D-printed samples, no preparation of the specimens' surface was

a) Trabecular Structure (TS)
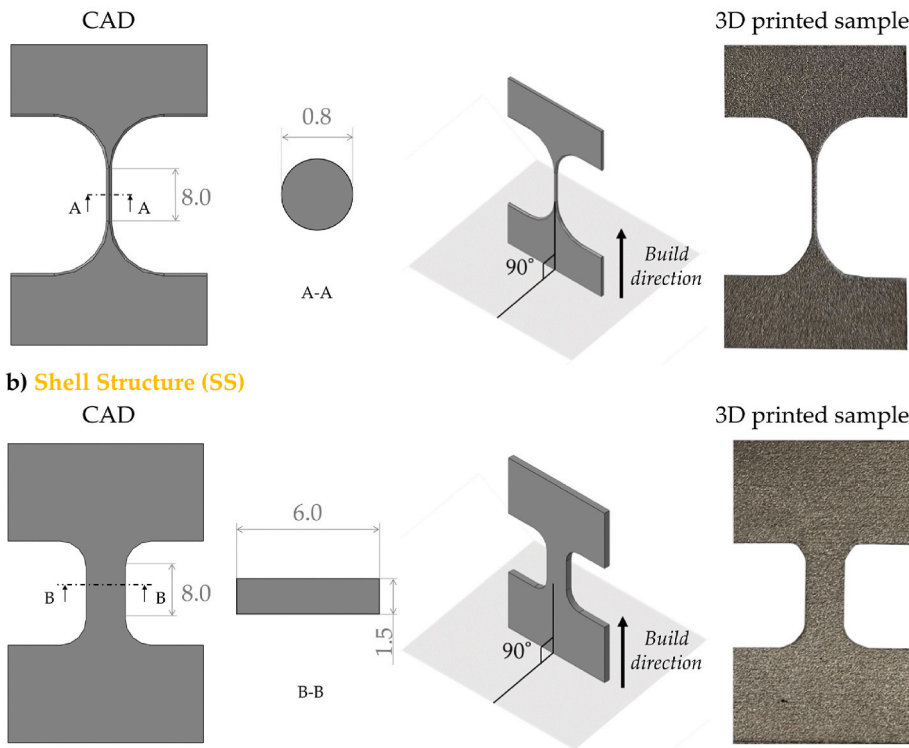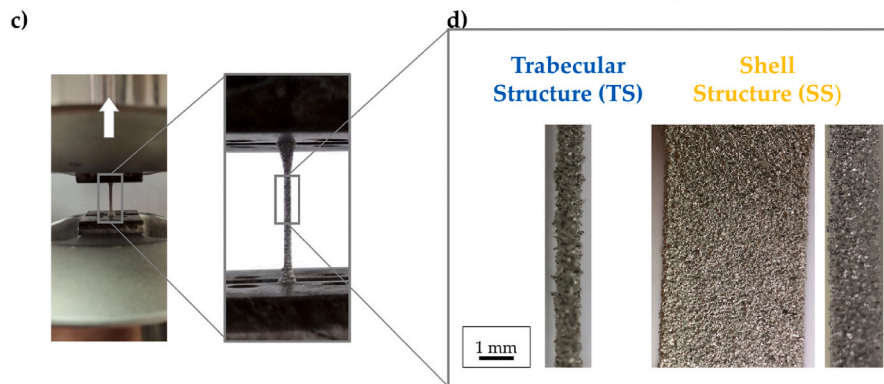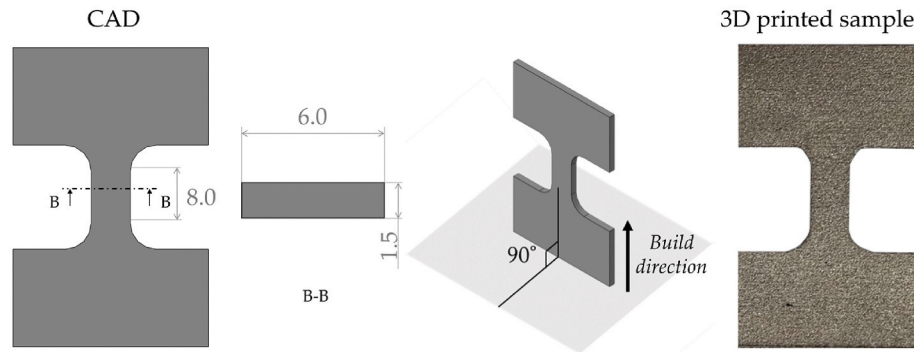

b) Shell Structure (SS)

Fig. 2. EBM manufactured Ti6Al4V dog-bone samples representing the typical size of (a) Trabecular Structure (TS) and (b) Shell Structure (SS). CAD drawings of the samples (left), schematic representation of the building direction (middle), and 3D printed samples (right). Dimensions are reported in mm. (c) Characterization of Ti6Al4V dog-bone samples: example of a representative uniaxial tensile test performed on a TS sample, with detail about its positioning with respect to the grips of the testing machine. (d) Optical images of the external surface of the gauge length: only one view is depicted for TS sample, representative of its diameter; two views are depicted for SS sample, to appreciate its width and thickness. Please, refer to the electronic on-line version of this article to appreciate the color code.

required. Optical images were acquired during testing using *Canon EOS 6D* digital camera (20.2 MP) and post-processed with the NCorr MAT-LAB software, exploiting Image Processing Toolbox (Blaber et al., 2015); displacements and strains within the gauge length were derived. DIC analysis showed that the FEA approach was able to predict the deformations of the gauge length, with a percentage error lower than 5%. Further, the results show both approaches to be valid options for measuring the strains of thin specimens, where the reduced dimensions prevent the use of extensometers. Further, the results show both approaches to be valid options for measuring the strains of thin specimens, where the reduced dimensions prevent the use of extensometers. However, FEA avoids the need to use ad-hoc optical instrumentation to acquire samples' images during testing together with specialized software to post-process the images (La Barbera et al., 2021).

2.2. FE modeling of the prostheses

Once the material parameters had been identified, the FE models of the acetabular and hemipelvis prostheses were developed. In this regard, Adler Ortho SPA provided the CADs of both implants, used to manufacture the corresponding physical samples, and the CADs of each

trabecular cell unit (indicated in the following as RVE, Representative Volume Element).

As regards the trabecular parts, the AEH theory was applied. The RVE of each trabecular design was imported in *Abaqus/Standard 2020* (Dassault Systèmes Ri, Simulia Corp. Providence, RI, USA) to discretize using linear tetrahedral elements (C3D4). Preliminarily, a mesh-sensitivity analysis was performed to solve the homogenization problem. The mesh size was considered adequate when the maximum percentage difference between the homogenized stiffness matrix ($\overline{D}$) of two consecutive meshes was lower than 1%. Following, the regions of the prosthesis occupied by the different trabeculated structures were modeled as continuum solids assigning homogenized mechanical properties to the corresponding trabecula. To this aim, the CAD models of both prostheses were modified accordingly using Boolean operations. The resulting solid parts were discretized in *Altair HyperMesh* (Altair Engineering, Troy, MI, USA) using linear C3D4 elements. Then, a mesh sensitivity analysis was performed. The mesh sizes were considered adequate when the maximum percentage differences of the von Mises stress and the principal stresses at specific locations of the prosthesis of two consecutive meshes were lower than 5%.

To quantify the influence of the size-effect on the mechanical

properties of the 3D printed material, thus highlighting the differences with respect to the works available in the literature, two versions of the FE model of the two prostheses were built (Fig. 1d).

- *Acetabular Model – Scale-Dependent Material (AM-SDM)* and *Hemi-pelvis Model – Scale-Dependent Material (HM-SDM)*: size-dependent mechanical properties (characterized as indicated in **2.1.**) were used for the solid parts and for calculating the homogenized properties of the trabecular structures;
- *Acetabular Model – Scale-Independent Material (AM-SIM)* and *Hemi-pelvis Model – Scale-Independent Material (HM-SIM)*: the mechanical properties of the standard Ti-alloy (conventional elastic modulus of 110 GPa (Majumdar et al., 2008; Wright et al., 2016; Schuh et al., 2007)) were used for the solid parts and for calculating the homogenized properties of the trabecular structures. This approach is commonly used in the literature (Rahimizadeh et al., 2018; Wojnicz et al., 2021; Moussa et al., 2020; Mehboob et al., 2020)).

2.3. Experimental measurements and virtual predictions of the implants' stiffness and local deformations

Experimental and numerical analyses were used to evaluate the stiffness and the local deformations of both devices. Two different loading configurations were considered to better characterize the contributions of the different materials. The acetabular prosthesis was positioned on ad-hoc support and loaded in compression with a spherical pin (Fig. 3a, left panel): the main relevant metal structures, both the trabecular filler (*TF*), the interface trabecular filler (*IF*), and the shell structure (*SS*) were encompassed during testing. The hemipelvis prosthesis was fixed with five screws to ad-hoc support and loaded on a cantilever beam fashion with a spherical pin applying flexion (Fig. 3b, left panel): here, the shell structure (*SS*) and the trabecular filler (*TF*) were extensively loaded, while the trabecular interface structure (*TI*) was less involved in the test. All the external supports were designed to be conforming to the corresponding external surfaces of the prostheses and were milled machined in steel by Adler Ortho.

The experiments were performed in displacement control using an *MTS 858 MiniBionix testing machine* (MTS System Inc., Minneapolis, MN) and setting a rate of 1 mm/min. The experimental protocol consisted of 5 loading-unloading cycles needed to reach a stable response. Since only one sample for each device was available, the prostheses were adequately loaded to avoid plasticity or damage. Each experiment was repeated three times to ensure a repeatable response.

The resulting force-displacement curves were post-processed and the macroscopic implant stiffness (K) calculated as the slope of the force-displacement curve between 1500 N and 2000 N (for acetabular prosthesis) and from 300 N to 500 N (for hemipelvis prosthesis) of the last loading cycle.

During the test, local strains in the devices were measured using Strain-Gauge (SG) rosettes (N32-FA-1-120-11-VS3; Showa Measuring Instruments Co., Ltd., Japan). To ensure adequate attachment of the SG rosettes on the prostheses, specific continuous solid parts were chosen while paying attention to avoid sharp corners and discontinuities at the interface between structures having different material behaviors. Therefore, they were attached to suitable areas of *SS* for both devices (see the detail of Fig. 3b, left panel). Compensation of thermal effect in the SG rosettes was achieved using a half-bridge Wheatstone configuration with a dummy specimen. The SG rosettes were connected to an MX840B (HBM, Darmstadt, Germany) amplifier system. From the local measurements, the maximum ($\varepsilon_{MAX,Prin}$) and the minimum ($\varepsilon_{MIN,Princ}$) principal strains were derived at peak force (2000 N and 500 N, respectively, for the acetabular and the hemipelvis prosthesis). For the evaluated quantities, average values and standard deviation were calculated.

Following, the tests were simulated in *Abaqus/Standard 2020,* and the numerical results were compared with the experimental ones. Fig. 3, right panels, show the finite element models of the experiments. When modeling the fixation of the prosthesis to the base, the screw head and the threaded part were simplified to cylinders, and the bolt effect was neglected. The accuracy of the implants' FE models was assessed by evaluating the implant stiffness and the local strains in the devices. As for the deformations, the maximum and the minimum principal strains were calculated with the FE models roughly the same regions where SG rosettes were applied on the *SS* parts of the physical samples.

a) Acetabular prosthesis
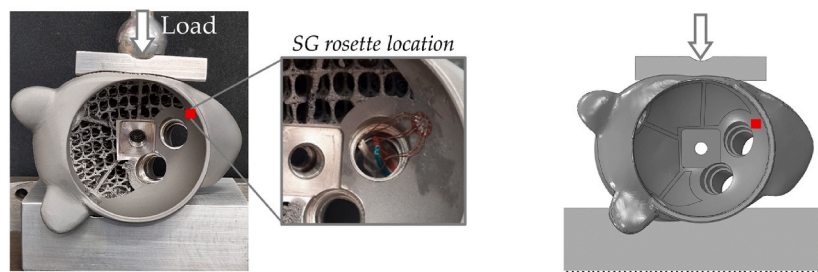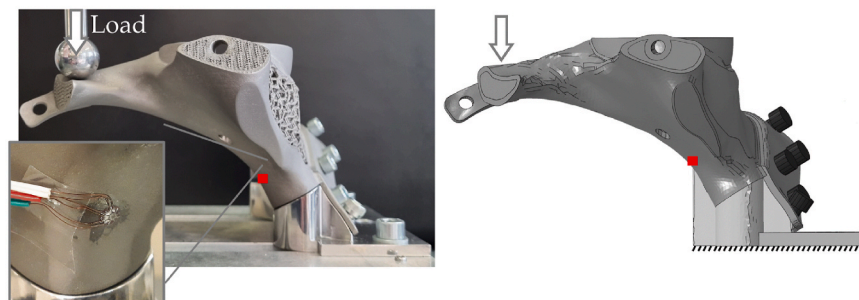

b) Hemipelvis prosthesis

Fig. 3. Experimental test setups (left) and numerical FE models (right) to assess the reliability of the developed FE models of (a) the acetabular prosthesis and (b) the hemipelvis prosthesis. Strain Gauges rosettes were applied on each prosthesis to compare the local principal strains.
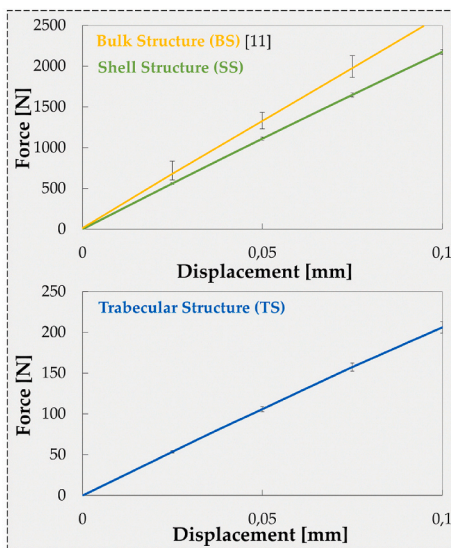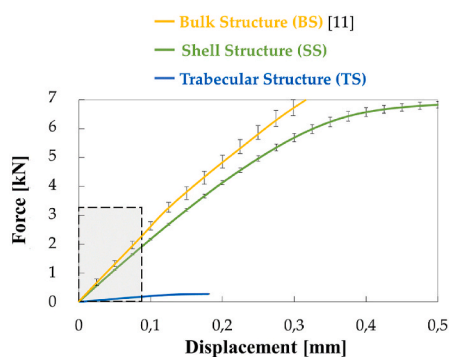
3. Results

The current section firstly reports the results about the material characterization of Ti6Al4V dog-bone samples manufactured by the EMB technology in different sizes. A coupled experimental-numerical approach was followed to determine the corresponding elastic modulus. Secondly, the experimental validation of the developed FE models of the acetabular and hemipelvis prostheses is shown. Both macroscopic (overall implant stiffness) and microscopic (local strain distribution) were evaluated.

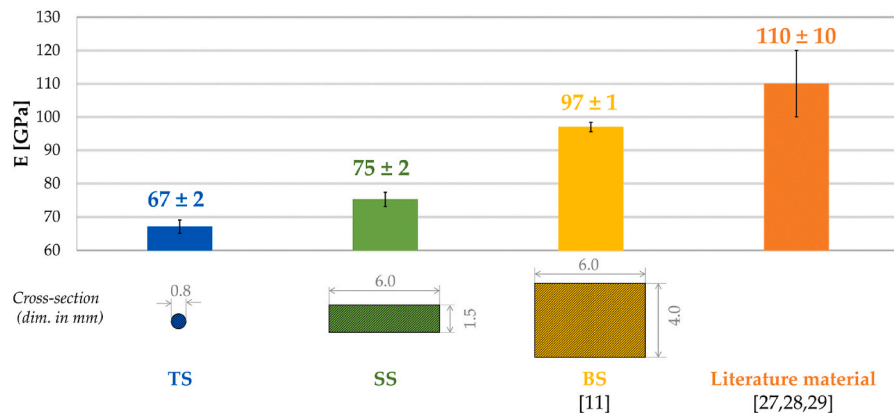### 3.1. Material characterization at different scales

Due to the uncertainties in manufacturing thin 3D-printed products, the evaluation of the cross-section dimension is fundamental in determining the elastic modulus. Except for a few measures, a global underestimation of gauge length's transversal dimension was observed with respect to the nominal one for both *TS* and *SS* dog-bone specimens. Namely, *TS* samples reported an average strut thickness equal to 0.76 mm ± 0.05 mm, underrating the nominal dimension (0.80 mm) by 5%. The *SS* samples showed average dimensions of (5.95 mm ± 0.03 mm) x (1.47 mm ± 0.04 mm), underrating the nominal ones (6 mm × 1.5 mm) by 2%.

Fig. 5 shows the average experimental force-displacement curves of the uniaxial tensile tests for *TS* and *SS* samples (Fig. 4a); the average curves and their standard deviation have been calculated and plotted. The data were post-processed to calculate the elastic moduli (E) for *TS* and *BS*, which are compared with the elastic modulus of *BS*,

characterized in a previous work (La Barbera et al., 2019), and of the standard Ti-alloy (Majumdar et al., 2008; Wright et al., 2016; Schuh et al., 2007) (Fig. 4b).

3.2. FE modeling of the prostheses

The characterized elastic moduli (accurate material) and the standard Ti-alloy properties (simplified material) were assigned to the discretized models of both prostheses to develop *AM-SDM*, *HM-SDM* with the accurate material description, and *AM-SIM*, *HM-SIM* with the simplified material description. Namely, the accurate material parameters are reported in Fig. 5 for each metal structure of relevance.

It is noteworthy that the homogenized stiffness matrixes of the simplified material can be scaled by the ratio between the simplified and the accurate material (110 GPa/67 GPa), given the linear dependence between E and the parameters of the matrix.

3.3. Experimental measurements and virtual predictions of the implants' stiffness and local deformations

Table 1 summarizes the experimental-numerical comparison for the acetabular and hemipelvis prostheses regarding stiffness and local deformations.

The results show that, in general, the numerical models based on simplified material properties (*AM-SIM* and *HM-SIM*) overestimate about 60% of the global stiffness of the implant while underestimating 19% ÷ 33% of the maximum strains and overestimating 32% ÷ 43% of the minimum strains compared to experiments. Conversely, the

a) Uniaxial tensile tests

b) Elastic modulus

Fig. 4. Experimental force-displacement curves (average curves with standard deviation) obtained within the uniaxial tensile tests performed on SS and TS samples. (b) Elastic modulus (average curves with standard deviation) was identified for the main relevant metal structures involved in the investigated prostheses: from left to right, TS (blue) and SS samples (green) were characterized in the current work, while BS samples (yellow) were characterized in a previous work (La Barbera et al., 2019). For each sample, the corresponding cross-section is compared. The identified material properties were compared with the conventional Ti-alloy available in the literature (orange) (Majumdar et al., 2008; Wright et al., 2016; Schuh et al., 2007). Please, refer to the electronic on-line version of this article to appreciate the color code.
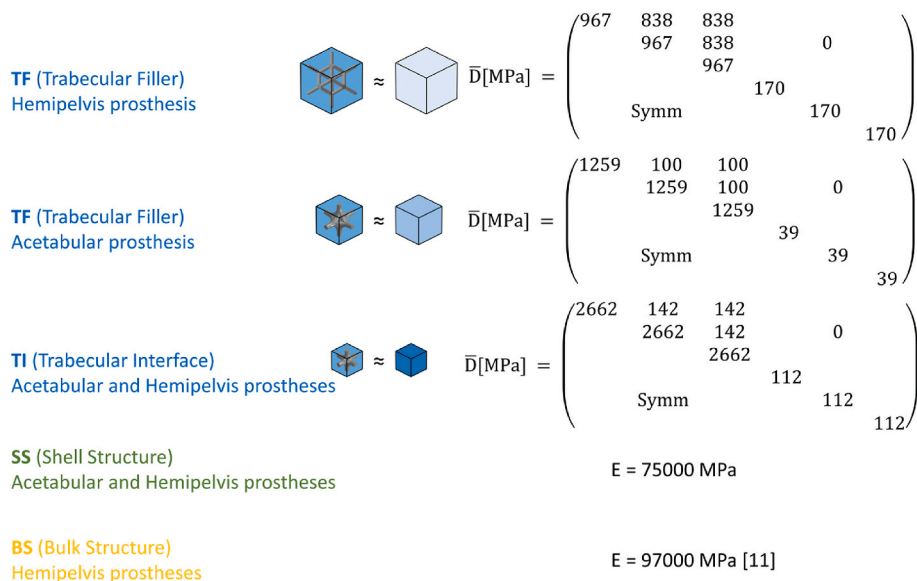
TF (Trabecular Filler)
Hemipelvis prosthesis

$$\bar{D}[MPa] = \begin{pmatrix} 967 & 838 & 838 & & & \\ & 967 & 838 & & 0 & \\ & & 967 & & & \\ & & & 170 & & \\ & Symm & & & 170 & \\ & & & & & 170 \end{pmatrix}$$

TF (Trabecular Filler)
Acetabular prosthesis

$$\bar{D}[MPa] = \begin{pmatrix} 1259 & 100 & 100 & & & \\ & 1259 & 100 & & 0 & \\ & & 1259 & & & \\ & & & 39 & & \\ & Symm & & & 39 & \\ & & & & & 39 \end{pmatrix}$$

TI (Trabecular Interface)
Acetabular and Hemipelvis prostheses

$$\bar{D}[MPa] = \begin{pmatrix} 2662 & 142 & 142 & & & \\ & 2662 & 142 & & 0 & \\ & & 2662 & & & \\ & & & 112 & & \\ & Symm & & & 112 & \\ & & & & & 112 \end{pmatrix}$$

SS (Shell Structure)
Acetabular and Hemipelvis prostheses

$E = 75000$ MPa

BS (Bulk Structure)
Hemipelvis prostheses

$E = 97000$ MPa [11]

Fig. 5. *Material properties assigned to the main relevant metal structures involved in the acetabular and the hemipelvis prosthesis: trabeculated and solid parts. The trabeculated parts (Interface Trabecular Structure, Filler Trabecular Structure) were homogenized (starting from an elastic modulus of 67 GPa), and the corresponding stiffness ($\bar{D}$) matrixes were calculated. The solid parts featured an elastic modulus of 75 GPa (Shell Structure), identified in the current work, and 97 GPa (Bulk Structure), identified in a previous work (La Barbera et al., 2019). Please, refer to the electronic on-line version of this article to appreciate the color code.*

Table 1
Comparison between experimental tests (EXP) and numerical simulations (AM-SIM, AM-SDM, HM-SIM, HM-SDM) for the acetabular and the hemipelvis prosthesis. Evaluation of the average implants' stiffness (K [N/mm]), and the average maximum ($\varepsilon_{MAX,Princ}$ [µm/m]) and minimum ($\varepsilon_{MIN,Princ}$ [µm/m]) local deformations. Data for the experiments and the numerical models are reported in terms of average values ± standard deviation (as needed), or percentage differences of each numerical model vs. experiments.

		K [N/mm]	$\varepsilon_{MAX,Princ}$ [µm/m]	$\varepsilon_{MIN,Princ}$ [µm/m]
Acetabular prosthesis	*EXP*	20456 ± 559	397 ± 22	−434 ± 19
	AM-SIM	32878	267 ± 37	−266 ± 28
	AM-SIM vs. EXP	*+61%*	*−33%*	*+43%*
	AM-SDM	20754	406 ± 57	−395 ± 42
	AM-SDM vs. EXP	*+2%*	*+2%*	*+9%*
Hemipelvis prosthesis	*EXP*	1106 ± 63	50 ± 5	−483 ± 6
	HM-SIM	1805	41 ± 7	−329 ± 31
	HM-SIM vs. EXP	*+63%*	*−19%*	*+32%*
	HM-SDM	1250	46 ± 11	−469 ± 41
	HM-SDM vs. EXP	*+13%*	*−8%*	*+3%*

numerical model based on accurate material properties (*AM-SDM* and *HM-SDM*) provides a better agreement with experiments, with a slight overestimation of the global stiffness (only 2% with *AM-SDM*, 13% with *HM-SDM*), and a better agreement with principal strains (always <9% compared with experiments).

4. Discussion

To date, custom orthopedic prostheses are a well-established example of additive manufacturing production. They are characterized by complex designs, in terms of both morphology and materials at different scales (starting from the order of hundreds of microns), which hinder the numerical modeling of the prostheses if computational tools are used to investigate realistic scenarios, such as the device's implant and loading transmission to the surrounding bone. Starting from two patient-specific pelvis prostheses manufactured by EBM and characterized by both solid and trabeculated parts, the current study aims at evaluating the influence of the mechanical response of scaled-dependent materials on the implant's mechanical behavior in terms of global stiffness and local deformations within the devices.

4.1. Scale-dependent material characterization: experimental tests and finite element analyses

As reported in the literature, the mechanical properties of 3D-printed materials are slightly lower than the properties of the bulk material. In accordance with recent studies (Murchio et al., 2021), this reduction is much more evident in structures with dimensions close to the resolution (i.e. accuracy limit) of the 3D printer, as it is the case of the thin struts present in the trabecular structure. In the current study, the material characterization outlined a reduction of the elastic modulus with the decrease of the cross-section dimensions compared to the conventional Ti6Al4V (110 GPa). Namely, the elastic modulus decreased by 40% and 35% for *TS* (nominal diameter of 0.8 mm) and *SS* samples (nominal dimensions of 6 mm × 1.5 mm), respectively (Fig. 4). This evidence suggests a scale-dependent reduction of the elastic modulus for thin 3D-printed samples. This behavior is in agreement with previous reported work (Sergueeva et al., 2009; Dzugan et al., 2018; Murchio et al., 2021; De Luca et al., 2021). Murchio et al. (2021) characterized only one-scale Ti6Al4V specimens (nominal diameter of 0.6 mm) produced with laser powder bed fusion. They reported an effective young modulus of 80 GPa, 20% larger with respect to the 67 GPa found in this work, despite the lower dimension of their samples, 0.6 mm vs. 0.8 mm nominal diameter for *TS* samples; however, when comparing different building directions, they found an elastic modulus even lower than in the present study (32 GPa was found for samples manufactured at a 45° building orientation vs. 67 GPa found in the current study). Dzougan et al. (Dzugan et al., 2018) reported results closer to the present study, with an elastic modulus of about 60 GPa for Ti6Al4V specimens obtained via selective laser melting (SLM) with a nominal diameter of 0.6 mm. Interestingly, Phutela et al. (2020) reported increasingly higher elastic modulus for dog-bone Ti6Al4V SLM specimens with rectangular cross-sections (5 × 2 mm^2) approaching the sizes of *SS* samples tested here and *BS* samples tested in previous work (La Barbera et al., 2019), but keeping below the conventional values expected for Ti6Al4V. In fact, they considered 1 × 2 mm^2, 2 × 2 mm^2, 3 × 2 mm^2, 4 × 2 mm^2, and 5 × 2 mm^2 (nominal size), measuring an elastic modulus, respectively, of 82, 90, 94, 97, and 96 GPa, in perfect agreement with the results reported in the present work. The differences in the reported values could be associated with the different 3D printing technology, process parameters, and powder characteristics or with the fact that the elastic modulus was

calculated based on the minimum observed cross-section areas, unlike an average value used in the present work. Despite the outlined differences and conscious of the still-open issues on the mechanical properties of 3D-printed products, possibly related with microstructural changes and the presence of internal defects (Sergueeva et al., 2009; Dzugan et al., 2018; Murchio et al., 2021; De Luca et al., 2021), the obtained results can be deemed consistent with previous literature data for the intended purpose of the study. Further, hypotheses on the cross-section shapes of dog-bone samples have been made during the material characterization. As outlined by Murchio et al. (2021), the shape of the cross section differs more from the nominal geometry as the printing angle decreases: the mismatch is higher if the samples are printed at an angle of 0° with respect to 90°. Nevertheless, it is reasonable to assume circular cross-sectional shapes for the investigated samples since they were printed at a 90° building orientation, which guarantees a higher fidelity to the nominal cross-section shape.

Finally, as for the experimental tests, uniaxial tensile tests were performed, while the in-vivo trabeculae of the studied devices might also be subjected to flexion and torsion. Thus, a more involved material characterization should be performed, considering more complex loading conditions. Following, the identified material parameters could be assessed by testing simple lattice structures mimicking the trabeculated parts prior to testing the prostheses.

4.2. Custom prostheses' models: experimental tests and finite element modelling

Moving towards the device level, uncertainties in the production of the implants are higher and less controllable than the 3D printing of the investigated Ti6Al4V dog-bone samples. For instance, the orientation of the trabecular cell units is different in different parts of the prosthesis, resulting in a variability in the shape and dimensions of the cross-section of the struts composing the trabecular cells. This may lead to a heterogeneous elastic modulus distribution within the same trabecular structure. A high-fidelity model should account for these peculiarities, thus requiring a more involved morphological and mechanical analysis of materials at different scales, an aspect that is out of the scope of the present study.

Once the materials were characterized, FE models of the prostheses were developed using the AEH approach to numerically model the trabeculated parts. Following, experimental-numerical tests were designed to assess the identified scale-dependent material. In this regard, differences were highlighted with respect to the works available in the literature, which follow a scale-independent material to model 3D printed prostheses with trabeculated parts (Ghosh et al., 1996; Rahimizadeh et al., 2018; El Halabi et al., 2011; Turunen et al., 2020; Wojnicz et al., 2021). The comparison was made on two levels: i) a global evaluation of the implants' stiffness and ii) a local evaluation of the deformations.

The tests were meant to test the main relevant metal structures, thus the characterized materials. In detail, the compressive experiment on the acetabular prosthesis involved all materials of interest: both the trabecular filler (*TB*) and the trabecular interface parts (*TI*) and the shell structure (*SS*). Rather, the cantilever bending experiments on the hemipelvis prosthesis barely involved the trabecular interface part, which in any case was tested with the other device. Therefore, a different loading modality and constraints result in significantly different stiffness values between the acetabular and the hemipelvis prostheses since the loading modality influences this mechanical parameter.

A first comparison shows how all the FE models overestimate the experimental stiffness (Table 1). Indeed, in the numerical simulation, this parameter is highly affected by the description of the boundary conditions used to constrain the prostheses during the experiments and the introduced contact between the devices and the loading pin. This is more evident for the hemipelvis prosthesis, which presents a more complex setup, including ad-hoc support and screws. In this regard, the model accurately describes the contact surfaces and the support

structure but introduces a simplification when modeling the screws (i.e. threaded part and bolt effect were both neglected).

Comparing the scale-independent simplified material models (*AM-SIM* and *HM-SIM*) with the scale-dependent accurate material ones (*AM-SDM* and *HM-SDM*), differences of up to a 60% between the numerical simulation and experiments were found for the models following the literature approach i.e., the young modulus of the bulk material is used to determine the effective properties of the trabecular structures and on all solid parts of the prosthesis. This results in lower maximum local strain of 33% (for *AM-SIM*) and 19% (for *HM-SIM*) and higher minimum deformation of 43% (for *AM-SIM*) and 32% (for *HM-SIM*). These results support that the elastic properties of the standard Ti-alloy cannot be used to describe the macro and microscopic behavior of a prosthesis with trabecular structures produced by additive manufacturing. This also indicates that a proper material characterization of the metal structures involved in 3D printed trabecular implants is required, given the impact of the peculiar additive manufacturing process on the elastic material properties. In this regard, when the differences in the young modulus at different scales are taken into account, differences of 2% for the implants' stiffness and less than 10% for the local deformations were obtained for the *AM-SDM* model. For the hemipelvis prosthesis, *HM-SDM* model, the difference in the stiffness was slightly over the 10%, maybe partially due to the more complex experimental setup that was numerically simplified as for the screws and the implant-setup contact, as described above. However, the analysis of the local strains (lower than 10%) shows a good agreement with experiments for the *HM-SDM* model.

To conclude, despite the discussed approximations, the numerical-experimental comparison undoubtedly demonstrates how an appropriate material characterization is needed to properly describe FE models of 3D printed implants characterized by a complex material distribution at different scales. In this regard, and looking at the literature, the current study outlined and overcame a limitation of the works focusing on the numerical modeling of these devices. However, another important limitation exists both in the literature and in the present study regarding the use of the AEH approach to model trabeculated parts. This method assumes that the RVE at the basis of a lattice structure has an infinitely periodic structure in space; this hypothesis may be inaccurate in the presence of a low, or even fractional, number of cells. A more accurate analysis should investigate the effect of the highlighted issues on the mechanical performance of homogenized lattice structures.

Finally, looking at the intended objective of the study, the highlighted limitations appear to slightly affect the global stiffness of the devices and the local deformations in the linear elastic range. However, further experimental tests should be designed, investigating other mechanical properties of the implants (i.e. static strength, fatigue resistance), which may require a more detailed description of the trabecular structure well beyond the elastic range and including fatigue loading. Thereby, the proposed approach would be assessed more thoroughly. In this perspective, the prostheses' implant in patient-specific anatomies could be simulated to support and improve the design and optimization phases. In view of these simulations, a more rational meshing strategy should be investigated, in particular for complex models including contacts among the prosthesis and the surrounding pelvic bone.

Last but not least, in this work, optical methods have been used to characterize the geometry of the samples. A more systematic analysis using microCT technology, as carried out in a work by Murchio et al. (2021) will provide an accurate representation of the geometry of the sample, including any internal defects, allowing for a more exhaustive material characterization.

5. Conclusion

The current study falls within the field of additive manufacturing exploited to produce custom prostheses for orthopedic applications. In this regard, the influence of the mechanical properties of different metal

structures (solid and trabecular parts) on the stiffness and local deformations of two custom-made prostheses was investigated.

The main findings of the current work can be summarized as follows.

- the elastic modulus decreased by 40% and 35% for *TS* (nominal diameter of 0.8 mm) and *SS* samples (nominal dimensions of 6 mm × 1.5 mm), respectively, with respect to the bulk elastic modulus (110 GPa);
- the use of a bulk elastic modulus led to an implant stiffness overestimation of 61% and 63% for the acetabular and the hemipelvis prosthesis, respectively;
- an appropriate scale-dependent material description is needed to develop reliable FE models describing the mechanical stiffness of 3D printed implants.

CRediT authorship contribution statement

Francesca Danielli: Writing – review & editing, Writing – original draft, Visualization, Software, Methodology, Investigation, Data curation. **Luca Ciriello:** Writing – review & editing, Writing – original draft, Visualization, Validation, Software, Methodology, Investigation, Formal analysis, Data curation. **Luigi La Barbera:** Writing – review & editing, Writing – original draft, Visualization, Validation, Supervision, Software, Methodology, Investigation, Formal analysis, Data curation, Conceptualization. **Jose Felix Rodriguez Matas:** Writing – review & editing, Writing – original draft, Supervision, Software, Project administration, Methodology, Funding acquisition, Conceptualization. **Giancarlo Pennati:** Writing – review & editing, Supervision, Resources, Project administration, Methodology, Funding acquisition, Conceptualization.

Declaration of competing interest

The authors declare the following financial interests/personal relationships which may be considered as potential competing interests:

Giancarlo Pennati reports financial support and equipment, drugs, or supplies were provided by Adler Ortho Srl.

Jose Felix Rodriguez Matas reports financial support and equipment, drugs, or supplies were provided by Adler Ortho Srl.

Giancarlo Pennati reports a relationship with Adler Ortho Srl that includes: consulting or advisory.

Jose Felix Rodriguez Matas reports a relationship with Adler Ortho Srl that includes: consulting or advisory.

Data availability

The data that has been used is confidential.

Acknowledgments

References

Arabnejad, S., Johnston, B., Tanzer, M., Pasini, D., 2017. Fully porous 3D printed titanium femoral stem to reduce stress-shielding following total hip arthroplasty. J. Orthop. Res. 35 (8), 1774–1783. https://doi.org/10.1002/jor.23445.

Blaber, J., Adair, B., Antoniou, A., 2015. Ncorr: open-source 2D digital image correlation matlab software. Exp. Mech. 55 (6), 1105–1122. https://doi.org/10.1007/s11340-015-0009-1.

De Luca, A., et al., 2021. Effects of the surface finish on thin specimens made by Electron beam melting technology. Macromol. Symp. 396 (1), 10–13. https://doi.org/10.1002/masy.202000307.

Dzugan, J., et al., 2018. Effects of thickness and orientation on the small scale fracture behaviour of additively manufactured Ti-6Al-4V. Mater. Char. 143 (April), 94–109. https://doi.org/10.1016/j.matchar.2018.04.003.

El Halabi, F., Rodriguez, J.F., Rebolledo, L., Hurtós, E., Doblaré, M., 2011. Mechanical characterization and numerical simulation of polyether-ether-ketone (PEEK) cranial implants. J. Mech. Behav. Biomed. Mater. 4 (8), 1819–1832. https://doi.org/10.1016/j.jmbbm.2011.05.039.

Ghosh, S., Lee, K., Moorthy, S., 1996. Two scale analysis of heterogeneous elastic-plastic materials with asymptotic homogenization and Voronoi cell finite element model. Comput. Methods Appl. Mech. Eng. 132 (1–2), 63–116. https://doi.org/10.1016/0045-7825(95)00974-4.

Hilton, T., Campbell, N., Hosking, K., 2017. Additive manufacturing in orthopaedics: clinical implications. SA Orthop. J. 16 (2), 63–67. https://doi.org/10.17159/2309-8309/2017/v16n2a9.

Ho, J.T., Wu, J., Huang, H.L., Chen, M.Y.C., Fuh, L.J., Hsu, J.T., 2013. Trabecular bone structural parameters evaluated using dental cone-beam computed tomography: cellular synthetic bones. Biomed. Eng. Online 12 (1), 1–10. https://doi.org/10.1186/1475-925X-12-115.

Iqbal, T., et al., 2017. Development of finite element model for customized prostheses design for patient with pelvic bone tumor. Proc. Inst. Mech. Eng. Part H J. Eng. Med. 231 (6), 525–533. https://doi.org/10.1177/0954411917692009.

Javaid, M., Haleem, A., 2018. Additive manufacturing applications in orthopaedics: a review. J. Clin. Orthop. Trauma 9 (3), 202–206. https://doi.org/10.1016/j.jcot.2018.04.008.

Kumar, R., Kumar, M., Chohan, J.S., 2021. The role of additive manufacturing for biomedical applications: a critical review. J. Manuf. Process. 64 (September 2020), 828–850. https://doi.org/10.1016/j.jmapro.2021.02.022.

La Barbera, L., Trabace, M., Pennati, G., Rodríguez Matas, J.F., 2019. Modeling three-dimensional-printed trabecular metal structures with a homogenization approach: application to hemipelvis reconstruction. Int. J. Artif. Organs 42 (10), 575–585. https://doi.org/10.1177/0391398819848001.

La Barbera, L., Wilke, H.J., Ruspi, M.L., Palanca, M., Liebsch, C., Luca, A., Brayda-Bruno, M., Galbusera, F., Cristofolini, L., 2021. Load-sharing biomechanics of lumbar fixation and fusion with pedicle subtraction osteotomy. Sci. Rep. 11 (1), 3595. https://doi.org/10.1038/s41598-021-83251-8.

Li, C., Pisignano, D., Zhao, Y., Xue, J., 2020. Advances in medical applications of additive manufacturing. Engineering 6 (11), 1222–1231. https://doi.org/10.1016/j.eng.2020.02.018.

Majumdar, P., Singh, S.B., Chakraborty, M., 2008. Elastic modulus of biomedical titanium alloys by nano-indentation and ultrasonic techniques-A comparative study. Mater. Sci. Eng. A 489 (1–2), 419–425. https://doi.org/10.1016/j.msea.2007.12.029.

Mehboob, H., et al., 2020. A novel design, analysis and 3D printing of Ti-6Al-4V alloy bio-inspired porous femoral stem. J. Mater. Sci. Mater. Med. 31 (9) https://doi.org/10.1007/s10856-020-06420-7.

Moussa, A., Rahman, S., Xu, M., Tanzer, M., Pasini, D., 2020. Topology optimization of 3D-printed structurally porous cage for acetabular reinforcement in total hip arthroplasty. J. Mech. Behav. Biomed. Mater. 105 (February) https://doi.org/10.1016/j.jmbbm.2020.103705.

Murchio, S., et al., 2021. Additively manufactured Ti–6Al–4V thin struts via laser powder bed fusion: effect of building orientation on geometrical accuracy and mechanical properties. J. Mech. Behav. Biomed. Mater. 119 (November 2020), 104495 https://doi.org/10.1016/j.jmbbm.2021.104495.

Phutela, C., Aboulkhair, N.T., Tuck, C.J., Ashcroft, I., 2020. The effects of feature sizes in selectively laser melted Ti-6Al-4V parts on the validity of optimised process parameters. Materials (Basel) 13 (1), 117. https://doi.org/10.3390/ma13010117.

Pianigiani, S., Verga, R., 2021. Finite element analysis of a 3D-PRINTED radial head prosthesis for verifying mechanical resistance in case of bone resorption. Orthop. Proc. 103-B (SUPP_1), 12. https://doi.org/10.1302/1358-992X.2021.1.012.

Rahimizadeh, A., Nourmohammadi, Z., Arabnejad, S., Tanzer, M., Pasini, D., 2018. Porous architected biomaterial for a tibial-knee implant with minimum bone resorption and bone-implant interface micromotion. J. Mech. Behav. Biomed. Mater. 78 (February 2017), 465–479. https://doi.org/10.1016/j.jmbbm.2017.11.041.

Schuh, A., Bigoney, J., Hönle, W., Zeiler, G., Holzwarth, U., Forst, R., 2007. Second generation (low modulus) titanium alloys in total hip arthroplasty. Mater. Werkst. 38 (12), 1003–1007. https://doi.org/10.1002/mawe.200700230.

Sergueeva, A.V., Zhou, J., Meacham, B.E., Branagan, D.J., 2009. Gage length and sample size effect on measured properties during tensile testing. Mater. Sci. Eng. A 526 (1–2), 79–83. https://doi.org/10.1016/j.msea.2009.07.046.

Turunen, M.J., et al., 2020. Sub-trabecular strain evolution in human trabecular bone. Sci. Rep. 10 (1), 1–14. https://doi.org/10.1038/s41598-020-69850-x.

Wang, Y., Arabnejad, S., Tanzer, M., Pasini, D., 2018. Hip implant design with three-dimensional porous architecture of optimized graded density. J. Mech. Des. Trans. ASME 140 (11), 1–13. https://doi.org/10.1115/1.4041208.

Wojnicz, W., Augustyniak, M., Borzyszkowski, P., 2021. Mathematical approach to design 3D scaffolds for the 3D printable bone implant. Biocybern. Biomed. Eng. 41 (2), 667–678. https://doi.org/10.1016/j.bbe.2021.05.001.

Wong, K.C., Kumta, S.M., Gee, N.V.L., Demol, J., 2015. One-step reconstruction with a 3D-printed, biomechanically evaluated custom implant after complex pelvic tumor

resection. Comput. Aided Surg. 20 (1), 14–23. https://doi.org/10.3109/10929088.2015.1076039.

Wright, J.O., Skelley, N.W., Schur, R.P., Castile, R.M., Lake, S.P., Brophy, R.H., 2016. Microstructural and Mechanical Properties of the, pp. 1656–1664.

Yan, L., Lim, J.L., Lee, J.W., Tia, C.S.H., O'Neill, G.K., Chong, D.Y.R., 2020. Finite element analysis of bone and implant stresses for customized 3D-printed orthopaedic implants in fracture fixation. Med. Biol. Eng. Comput. 58 (5), 921–931. https://doi.org/10.1007/s11517-019-02104-9.